Journal of Applied Electrochemistry **34**: 807–813, 2004.

Modeling of the current distribution in aluminum anodization

ROHAN AKOLKAR[1], UZIEL LANDAU[1]*, HARRY KUO[2] and YAR-MING WANG[2]
[1]*Department of Chemical Engineering, A.W. Smith Building, Case Western Reserve University, 10900 Euclid Avenue, Cleveland, OH 44106, USA*
[2]*Materials and Processes Laboratory, General Motors R&D, 30500 Mound Road, Warren MI, 48090, USA*
*(*author for correspondence: e-mail: uxl@po.cwru.edu)*

Received 1 November 2003; accepted in revised form 2 March 2004

Key words: aluminum, anodization, computer aided modeling, current distribution

Abstract

The growth of porous anodic Al_2O_3 films, formed potentiostatically in continuously stirred 15 wt.% H_2SO_4 electrolyte was studied as a function of the anodization voltage (14–18 V), bath temperature (15–25 °C) and anodization time (15–35 min). The variation of the anodic surface overpotential with the current density was measured experimentally. The film thickness at the more accessible portions of the anode was observed to increase with the anodization voltage and the bath temperature. However, the film thickness on the less accessible portions of the anode did not significantly change with the voltage or the bath temperature. This indicates that the anodization process at the more accessible regions is more strongly influenced by the surface processes than by the electric migration within the electrolyte. Furthermore, analysis confirms that the major portion of the film resistivity resides within a thin sub-layer that does not vary with the anodization time, and the growing anodic layer contributes only marginally to the overall film resistance. Computer aided design software was employed to simulate the current density distribution. For the range of process parameters studied, the electrochemical CAD software predicts accurately the measured thickness distribution along the anode.

List of symbols

A	Mott Cabrera parameter (A cm^{-2})
B	Mott Cabrera parameter (V^{-1})
E^0	Standard electrode potential (V)
F	Faraday's constant (96487 C mol^{-1})
h	Anodic oxide thickness (μm)
I	Total current (A)
i	Anodization current density (A cm^{-2})
l	Characteristic length (cm)
M_{ox}	Molecular weight of Aluminum oxide (g)
n	Number of electrons transferred during anodization
p	Porosity of Aluminum oxide
R_a^*	Specific surface resistance (Ω cm^2)
R_Ω^*	Specific ohmic resistance (Ω cm^2)
S	Anodic surface area (cm^2)
T	Anodization temperature (°C)
V	Anodization voltage (V)
w	Weight of anode specimen (g)
x, y	Coordinates of position on the anode surface

Greek

ε	Current efficiency during anodization
κ	Electrolyte conductivity (S cm^{-1})
η_a	Anodization surface overpotential (V)
η_Ω	Ohmic overpotential (V)
φ	Potential (V)

1. Introduction

Aluminum anodization is widely used in industry to impart abrasion resistance and corrosion protection to structural components. Anodization in H_2SO_4 electrolyte results in the growth of a porous oxide layer with a close-packed columnar hexagonal structure. The structural features of these porous anodic oxide coatings were investigated by Keller and co-workers [1]. These investigators examined the oxide structure using electron microscopy and established the dependence of pore density, pore diameter and volume on the forming voltage and the type of the electrolyte. Recent studies [2–4] have focused on analyzing the structural features of the porous anodic oxide and modeling its growth kinetics. In another related study [5], Patermarakis and Tzouvelekis developed a kinetic model for the oxide

growth on aluminum and derived a relationship between the oxide structural features, e.g. porosity, and the electrolyte concentration. In a recent article [6], Ono and Masuko reported measurements of the pore diameter and oxide porosity by pore-filling techniques. They observed that the oxide porosity decreases whereas the pore diameter increases marginally with the forming voltage for anodization in sulfuric acid. Other studies [7, 8] have focused on modeling current transients during constant voltage anodization.

The thickness of the oxide layer is often considered to be uniform across the anodized part due to the relatively high resistivity of the anodic barrier film, and consequently, the thickness distribution of the oxide film has not been the subject of much analysis. However, as shown here, anodized parts with complex or non-accessible features may experience large variations in the anodized layer thickness, often in critical regions such as grooves and cracks. We focus here on modeling the current density and the anodic oxide thickness distribution in the aluminum anodization process.

Characterizing the current density distribution is important for identifying regions on the anodized part where low currents result in formation of thinner anodic oxide films that are not sufficiently strong and lack corrosion resistance. Effects of operating parameters including voltage, bath temperature, and anodization time on the thickness distribution are analyzed.

2. Experimental procedure

Porous anodic Al_2O_3 films were prepared by anodizing potentiostatically, AA 6111 specimens at voltages of 14, 16 and 18 V in a continuously stirred 15 wt.% H_2SO_4 electrolyte at bath temperatures of 15, 20 and 25 °C for anodization periods of 15, 25 and 35 min. Continuous agitation was maintained in the anodization cell to ensure a uniform temperature throughout the bath. The electrochemical cell [9] consisted of aluminum cathodes where hydrogen gas evolved. The cathodes were placed sufficiently far (15 cm) from the anodes to ensure that hydrogen bubbles do not reach the anode. The anode assembly, shown in Figure 1, consisted of two 48 cm × 10 cm aluminum specimens, each 0.1 cm thick, held at 0.8 cm spacing by two rubber side strips. The anode was immersed in the electrolyte to a depth of 43 cm The portion of the anode, which remained above the solution, was used to make electrical connections. This geometry was chosen to simulate an anodized part where certain portions thereof are highly accessible to current (e.g. the outer surface of the anode plates) while other portions are highly inaccessible to current (e.g. the interior surfaces of the two parallel anodes). The anode assembly could be easily disassembled and the oxide thickness distribution could be conveniently measured. This configuration also provides a uniform horizontal thickness distribution thus eliminating three-dimensional effects.

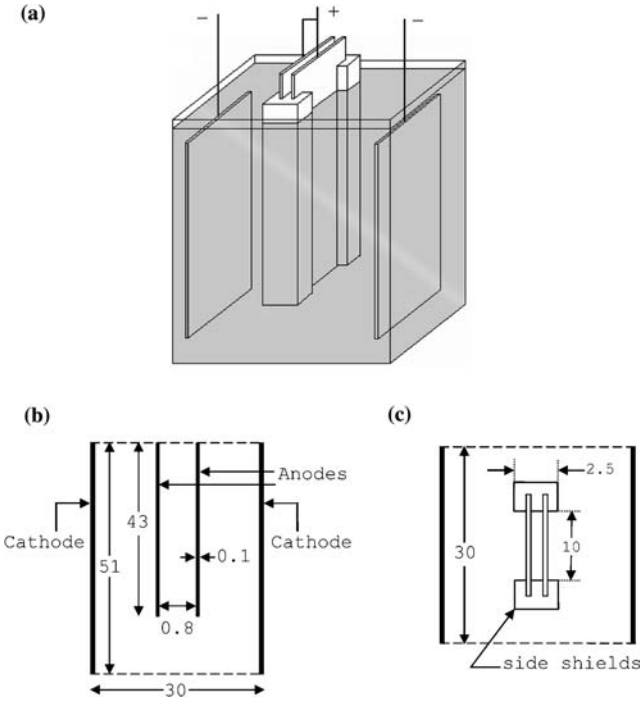

Fig. 1. (a) The electrochemical anodization cell. (b) Vertical cross-section of the cell, which was used for simulating the anodization current distribution. (c) Top view of the cell. All dimensions are in cm. Drawing not to scale.

3. Results and discussion

3.1. *Anodization kinetics*

In order to measure the anodization kinetics, only a single Al sheet was used as the anode. The potential difference between this Al sheet and a saturated calomel reference electrode, placed in close proximity (2–3 cm) to the sheet surface, was measured using a Hewlett Packard 34401A potentiometer. This potential corresponds primarily to the anodic overpotential for charge transfer across the oxide film. The contribution of the ohmic overpotential within the electrolyte is negligible (~100 mV), as compared to the surface overpotential (~10 V), owing to the sufficiently high electrolyte conductivity (0.55 S cm^{-1}) vs the high anodic film resistance. Mass transport overpotential was minimized by maintaining high agitation in the electrolyte. The anodic overpotential was measured at different current densities to generate the polarization curve. The experimental anodic polarization curves at different temperatures are shown in Figure 2. The dependence of the current density (i) on the anodic overpotential (η_a) can be represented by the Mott Cabrera [10] equation for high field ionic transport:

$$i = A \exp(B \cdot \eta_a) \tag{1}$$

where A and B are temperature dependent parameters. Fitting the polarization data at 20 °C in Figure 2, we obtain $A = 9.9 \times 10^{-4}$ A cm^{-2} and $B = 0.201$ V^{-1}.

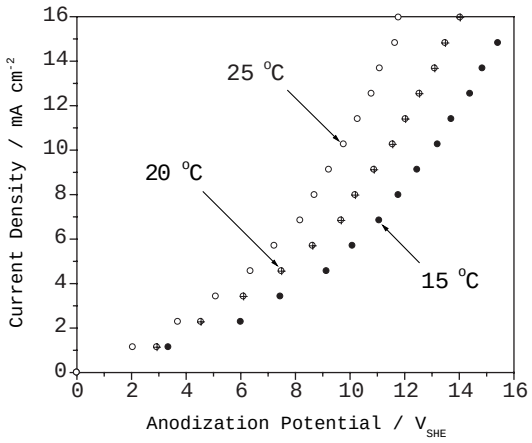

Fig. 2. Polarization data for aluminum anodization at different bath temperatures.

The specific resistance for the anodic surface processes can be represented as

$$R_a^* \equiv \frac{\partial \eta_a}{\partial i} = \frac{1}{B \cdot i} \quad [\Omega\,\mathrm{cm}^2] \tag{2}$$

The specific ohmic resistance is

$$R_\Omega^* \equiv \frac{\partial \eta_\Omega}{\partial i} = \frac{l}{\kappa} \quad [\Omega\,\mathrm{cm}^2] \tag{3}$$

In analogy to the Wagner number [11] we represent the ratio of the anodic surface resistance to the ohmic resistance as

$$Wa^{\mathrm{anod}} = \frac{\kappa}{B \cdot i \cdot l} \tag{4}$$

This dimensionless parameter is expected to be a measure of the thickness uniformity of the anodic film. $Wa^{\mathrm{anod}} > 1$ is indicative of dominance of the resistance associated with the oxide layer, which tends to level the layer, over the ohmic electrolyte resistance which is typically non-uniform. Considering the outer accessible surfaces of the anodes in the cell configuration shown in Figure 1, we take for the characteristic length $l \sim 15$ cm. Assuming typical anodization current density (i = 20 mA cm^{-2}), we find that $Wa^{\mathrm{anod}} = 9$. This indicates that the anodic film resistance is about nine times higher than the ohmic resistance on the accessible anode surfaces facing the cathodes and therefore is controlling the distribution and growth of the oxide layer on those surfaces.

3.2. *Modeling of the current distribution*

The potential within a well mixed electrolyte follows Laplace's equation [12]:

$$\nabla^2 \phi = 0 \tag{5}$$

Laplace's equation was solved numerically for the configuration shown in Figure 1, using a commercial computer-aided design software (CELL DESIGN®) [13], specifically designed for modeling electrochemical cells. The boundary condition applied at the anode was

$$\phi = V - E^0 - \eta_a(i) \tag{6}$$

where V is the anode voltage, E^0, is the standard electrode potential (~0.1 V) and η_a is the anodic overpotential measured experimentally as a function of the current density (Figure 2). These measured overpotentials at various current densities were entered into the CAD software to account for the electrode polarization. The software performs a least squares fit of the polarization data to the Butler–Volmer equation to provide optimized anodization kinetic parameters (A and B in Equation 1). These kinetic parameters are then used to compute the surface overpotentials during the numerical solution. Figure 3 shows a typical potential and current density distribution simulated for 25 min anodization at 16 V and 20 °C. In order to determine the current efficiency during anodization and the porosity of the resulting oxide film, 15 cm × 6.4 cm AA 6111 samples were anodized in a square cell configuration that provided uniform anodized layer thickness over the part. The samples were weighed before anodization (w_1) and after anodization (w_2). The oxide layer was subsequently dissolved by immersing the anodized samples in a well-stirred solution of chromic oxide and orthophosphoric acid at 90 °C for 20 min. This solution attacks only the oxide layer leaving the Al metal intact. The samples were weighed intermittently to verify complete oxide dissolution and their final weight (w_3) was recorded. The current I during anodization was also recorded. The current efficiency (ε) was calculated from

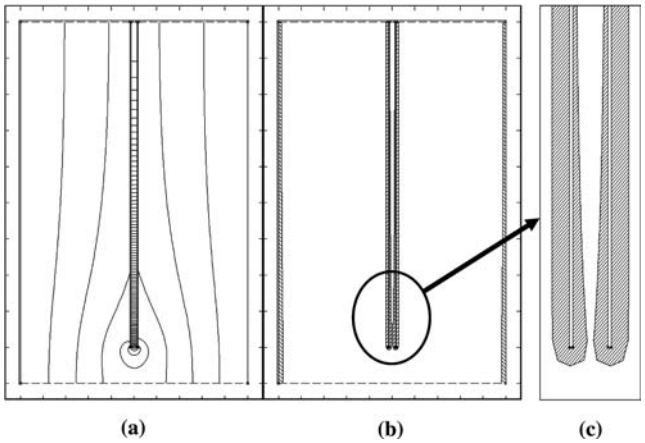

Fig. 3. (a) Potential distribution indicating significant potential drop in the region between the two anodized plates. (b) A current density map along the anodes indicating the oxide thickness distribution. The cross-hatched region is proportional to the current density. (c) Magnified view of the bottom of the anode assembly indicating the uniformity of the oxide on the more accessible external surfaces and the non-uniform distribution in the interior. Graphics were generated by CELL DESIGN® software. Parameters: $V = 16$ V, $\kappa = 0.55$ S cm^{-1} and polarization data of Figure 2.

$$\varepsilon = \frac{(w_2 - w_3)Fn}{M_{ox}It} \tag{7}$$

where M_{ox} is the molecular weight of aluminum oxide, t the anodization time, n the number of electrons transferred (=6) and F Faraday's constant. The current efficiency was observed to be about 68–72% depending on the operating conditions (V=14–18 V; T=15–25 °C). The low efficiency is due to the oxygen co-evolution at the anode coupled with the dissolution of the formed oxide. The porosity (p) of the oxide layer was estimated using the following equation:

$$p = 1 - \frac{\varepsilon M_{ox}It}{SFn\rho_{ox}h} \tag{8}$$

where S is the surface area of the sample (193 cm^2), ρ_{ox} the density of the compact oxide (3.97 g cm^{-3}) and h the measured oxide layer thickness. The anodized film thickness was measured using a Fischerscope multi measuring system. The observed porosity ranged between 28 and 33%, the lower limit corresponding to a lower anodization temperature of 15 °C and the upper limit corresponding to a higher anodization temperature of 25 °C. As indicated above, the current efficiency and the anodic oxide porosity do not change significantly in the range of operating conditions considered (V = 14–18 V; T = 15–25 °C). In an earlier study [3], it was reported that the anodic oxide growth rate varies linearly with the anodization current density, i.e. the constant of proportionality between the growth rate and the current density, which accounts for the current efficiency and the oxide structural properties, is independent of the current density and the anodization temperature and can be assumed to be constant. This indicates that the structural properties of the oxide film, e.g. the oxide porosity, are relatively unaffected by the current density. In the experiments discussed and the analysis presented below, we have also observed oxide growth rates varying linearly with the local current density, being relatively independent of the anodization time or the oxide thickness. Taking the average current efficiency as 70% (calculated from Equation 7) and the average porosity as 30% (calculated from Equation 8), and the current density distribution as provided by the solution of Equation 5, the oxide thickness distribution along the anode can be determined using Faraday's law

$$h(x,y) = \frac{\varepsilon M_{ox} i(x,y)t}{F\rho_{ox}(1-p)n} \tag{9}$$

where $h(x,y)$ is the oxide thickness as a function of position on the anode surface and $i(x,y)$ is the current distribution. All other parameters in Equation 9 are as defined above.

For measuring purpose, the distance along the anode was measured starting at the outer top position of the anode plate, following along the anode and ending at the top interior point of the anode between the two plates as indicated in Figure 4. Thickness measurements were taken at an interval of 5 cm. along the anode. At each position, five readings were taken and the average and standard deviation were calculated. The simulated oxide thickness distribution was compared to the experimental results. Figure 5 provides a comparison between experimental and modeling results for anodic oxide films formed at 16 V for 25 min. in H_2SO_4 electrolyte at 20 °C. As noted, the experimental results are in good agreement with the simulations.

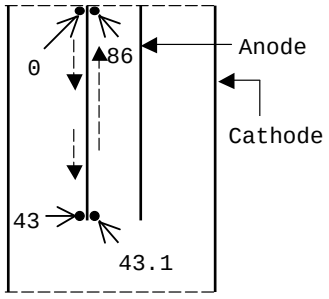

Fig. 4. Measurement positions along the anode. Numbers indicate distance (in cm) along the measuring path. Oxide thickness was measured along this path at 5 cm intervals.

3.3. *Effect of the anodization time*

Anodic oxide films on aluminum were formed at 16 V in a 15 wt.% H_2SO_4 electrolyte at 20 °C for different anodization periods. The experimental thickness distribution was compared to the simulated thickness distribution (Figure 6). Good agreement between experimental and CELL DESIGN's modeling results was observed. The oxide thickness was observed to

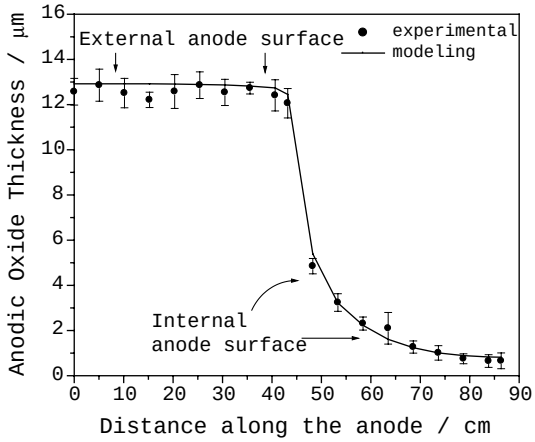

Fig. 5. Comparison between experiments and modeling (CELL DESIGN) for anodization at 16 V for 25 min (20 °C). The error bars indicate one standard deviation. The uniform oxide thickness for the 0–43 cm region corresponds to the more accessible outer faces. The large drop in thickness (43–86 cm region) corresponds to the internal surface. Parameters are same as in Figure 3.

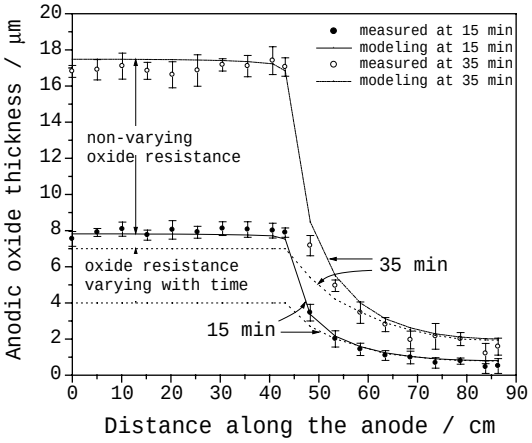

Fig. 6. Comparison between experiments (dots) and CELL DESIGN modeling (lines) for anodization assuming either a constant film resistance within a non-varying compact barrier layer or a distributed resistance throughout the film. Conditions: anodization at 16 V, 20 °C, for 15 and 35 min. Parameters: κ=0.55 S cm^{-1} and polarization data of Figure 2.

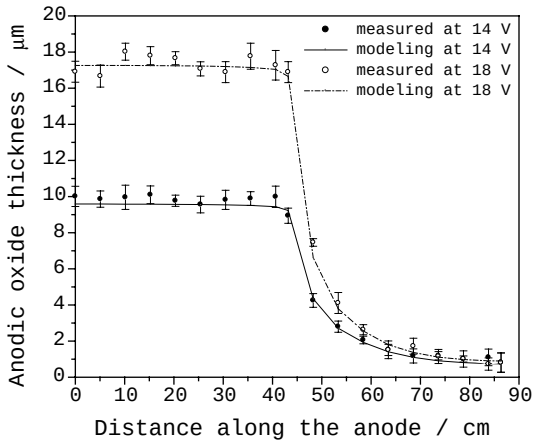

Fig. 7. Comparison between experiments and modeling for anodizing at different voltages at 20 °C for 25 min. Parameters: κ=0.55 S cm^{-1} and polarization data of Figure 2.

increase with time uniformly all along the part, indicating that the current efficiency and porosity do not significantly vary with time or with the anodic layer thickness. Furthermore, the linear increase in thickness with time indicates that the current density does not vary with time or with the oxide thickness. Since anodization was carried under potentiostatic conditions, this indicates that the film resistance, which dominates the process, does not vary, although the film thickness almost doubled. This is an indirect but compelling proof that almost the entire film resistance resides in a compact sublayer that does not change its resistance as the porous oxide grows. A thickness distribution was simulated using CELL DESIGN for the same conditions as above but assuming a resistive film growth with a resistivity of 1×10^6 Ω cm. The simulated distribution is shown in Figure 6 as a dotted curve. We observe that, in the case of a resistive film, not only does the film grow to a lower thickness under potentiostatic anodization but also, as expected, the thickness does not increase linearly with time. Simulations indicate that assuming a film resistance distributed across its entire thickness and therefore varying with anodization time, the oxide thickness on the outer, more accessible anode surface increased by a factor of only 1.75 when the anodization time was increased from 15 to 35 min, i.e. by a factor of 2.33.

3.4. *Effect of the anodization voltage*

Aluminum anodization was performed for 25 min at different DC anodization voltages and the oxide thickness was measured. The experimental thickness distributions were in good agreement (Figure 7) with the distributions simulated by CELL DESIGN.

The current density in anodization can be approximated as the ratio of the voltage driving force to the total resistance:

$$i = \frac{\Delta V - E^0}{R^*_\Omega + R^*_a} = \frac{\Delta V - E^0}{\frac{l}{\kappa} + \frac{1}{B \cdot i}} \tag{10}$$

Recognizing that $\Delta V >> E^0$, we can conclude that if the anodization process is controlled by the ohmic resistance (R^*_a is negligible in comparison to R^*_Ω), the current density (i) should be directly proportional to the applied voltage ΔV at all positions along the anode, since l and k are both independent of the current and voltage. However, from Figure 7, it is evident that an increase in the anodization voltage significantly affects the current density on the more accessible surfaces, i.e. increasing the anodization voltage from 14 to 18 V increases the anodic oxide thickness by about 70%. However, the current density on the less accessible interior surfaces remains essentially unaffected by the increase in voltage. This difference in the response of the current density to an increase in voltage is suggestive of a process in which the surface resistance, R^*_a, is significant. The dependence of i on ΔV when the kinetic resistance cannot be neglected is given by Equation 10.

Let V_1 and V_2 denote high and low anodization voltages, respectively,

$$V_1 = \eta_{a1}(i_1) + \eta_{\Omega 1}(i_1) \tag{11}$$

$$V_2 = \eta_{a2}(i_2) + \eta_{\Omega 2}(i_2) \tag{12}$$

As stated above, the standard potential is much smaller than either V_1 or V_2 and therefore assumed negligible. On the more accessible outer surfaces of the anode plates, we may assume that η_Ω is negligible in comparison to η_a. This assumption is supported by the simulations depicted in Figure 3(b); showing that most of the voltage drop in the electrolyte occurs within the narrow gap between the anodes. We can then approximate for the accessible outer surfaces the voltage ratio:

$$\frac{V_1}{V_2} = \frac{\eta_{a1}(i_1)}{\eta_{a2}(i_2)} = \frac{\ln(i_1/A)}{\ln(i_2/A)} \tag{13}$$

Therefore, an increase in voltage leads to a logarithmic increase in the current density. For $V_1 = 18$ V and $V_2 = 14$ V, $V_1/V_2 = 1.28$. From the thickness measurements, we determine a current density of about 26 mA cm^{-2} on the outer surface at 18 V and 14.4 mA cm^{-2} at 14 V. The right hand side of Equation 13 was computed to be 1.22, well in agreement with the voltage ratio.

3.5. *Effect of bath temperature*

Temperature affects the kinetics of ionic transport across the barrier layer. An increase in temperature enhances the ionic migration through the barrier film, increasing the current density and the deposit thickness. This effect was observed in the measured polarization curves (Figure 2) as well as in the deposit thickness profile (Figure 8). Anodic oxide films on aluminum were formed at 16 V for 25 min at different bath temperatures. The experimental thickness distribution was in good agreement with the simulated thickness distribution (Figure 8). From Figure 8, it is evident that an increase in the bath temperature significantly affects the current density on the more accessible surfaces, i.e. increasing the bath temperature from 15 to 25 °C doubles the anodic oxide thickness (10 μm for 15 °C and 20 μm for 25 °C). However, the current density on the less accessible interior remains essentially unaffected. This behavior is also suggestive of a process in which the surface resistance R_a^*, on the accessible surfaces is significant. The increase in temperature affects the kinetic parameter B in Equation 10. Let V_1 and V_2 denote high and low bath temperatures, respectively,

$$V_1 = \eta_{a1}(i_1, T_1) + \eta_{\Omega 1}(i_1, T_1) \tag{14}$$

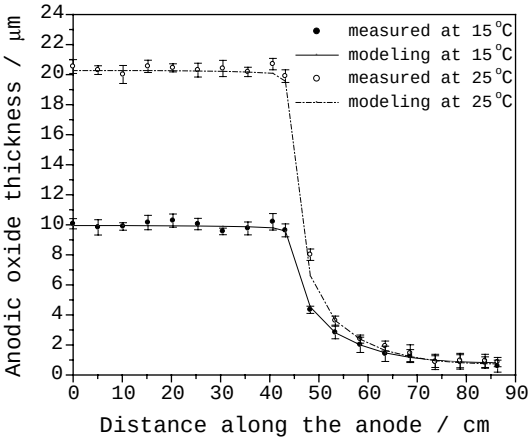

Fig. 8. Experimental and CELL DESIGN modeling results for anodization at 15 °C and 25 °C, applying 16 V for 25 min in H_2SO_4. Parameters: κ=0.55 S cm^{-1} and polarization data shown in Figure 2.

$$V_2 = \eta_{a2}(i_2, T_2) + \eta_{\Omega 2}(i_2, T_2) \tag{15}$$

On the more accessible outer surfaces of the anode plates, η_Ω is negligible,

$$\frac{V_1}{V_2} = \frac{\eta_{a1}(i_1, T_1)}{\eta_{a2}(i_2, T_2)} = \frac{\frac{1}{B_1}\ln\left(\frac{i_1}{A_1}\right)}{\frac{1}{B_2}\ln\left(\frac{i_2}{A_2}\right)} \tag{16}$$

For same anodization voltage, $V_1 = V_2 = 16$ V, and $V_1/V_2 = 1$. From the thickness measurements, we determine a current density on the outer surfaces of about 15.1 mA cm^{-2} at 15 °C and 30.6 mA cm^{-2} at 25 °C. From the temperature dependent parameters of the polarization curve ($A_1 = 7.54 \times 10^{-4}$ A cm^{-2}, $A_2 = 1.09 \times 10^{-3}$ A cm^{-2}, $B_1 = 0.1965$ V^{-1}, $B_2 = 0.2270$ V^{-1}), the right hand side of Equation 16 was computed to be 1.04 well in agreement with the voltage ratio.

4. Conclusions

The current distribution in aluminum anodization and the oxide layer thickness distribution were characterized using scaling analysis, numerical simulations and experiments in a test fixture that was specifically designed to incorporate highly accessible surfaces, and recessed, less accessible regions thus providing a highly non-uniform oxide distribution. A range of operating parameters including the voltage, anodization time and bath temperature was analyzed. The oxide layer thickness was observed to increase linearly with the anodization time at all locations along the anode indicating that the oxide layer is porous and the entire oxide resistance resides within a compact sublayer which does not grow with time or oxide thickness. It was also observed that the oxide thickness on the more accessible outer surface of the anode assembly increased significantly with the voltage and the bath temperature whereas the oxide on the less accessible regions did not increase appreciably with voltage and temperature. This suggests that the oxide growth on the more accessible regions was primarily controlled by the oxide film resistance whereas the anodization process on the less accessible portions of the anode was under a mixed control of ohmic transport within the electrolyte and the surface film resistance. A commercial electrochemical computer aided design software (CELL DESIGN) was used to simulate the anodization process. Close agreement was noted between the simulations and the experimental measurements.

Acknowledgement

General Motors Research & Development Center, Warren, MI is acknowledged for financial support. We also thank Dr. M. Verbrugge for helpful discussions.

References

1. F. Keller, M.S. Hunter and D.L. Robinson, *J. Electrochem. Soc.* **100** (1953) 411.
2. G. Patermarakis and K. Moussoutzanis, *Electrochim. Acta* **40**(6) (1995) 699.
3. G. Patermarakis, P. Lenas, Ch. Karavassilis and G. Papayiannis, *Electrochim. Acta* **36**(3/4) (1991) 709.
4. G. Patermarakis and K. Moussoutzanis, *J. Electrochem. Soc.* **142**(3) (1995) 737.
5. G. Patermarakis and D. Tzouvelekis, *Electrochim. Acta* **39**(16) (1994) 2419.
6. S. Ono and N. Masuko, *Surf. Coatings Technol.* **169–170** (2003) 139.
7. J.M. Albella, I. Montero, O. Sanchez and J.M. Martinez-Duart, *J. Electrochem. Soc.* **133** (1986) 876.
8. M.C. Jimenez, J.M. Albella, I. Montero and J.M. Martinez-Duart, *Electrochim. Acta* **34**(7) (1989) 951.
9. General Motors Engineering Standards GM9535P, March 1989.
10. L. Young, *Anodic Oxide Films* (Academic Press, London, 1961).
11. U. Landau, R.E. White and J. Newman (eds.), *in Proceedings of the D.N. Bennion Mem. Symp.*, (The Electrochemical Society Proceedings 94-9, 1994).
12. J.S. Newman, *Electrochemical Systems* (Prentice-Hall, NJ, 1973).
13. "CELL DESIGN", *Computer Aided Design Software for Electrochemical Cells*, L-Chem Inc., Shaker Heights, OH 44120.